The light subunit of mushroom Agaricus bisporus tyrosinase

Ismaya, Wangsa T.; Tandrasasmita, Olivia M.; Sundari, Syaripah; Diana, G.; Lai, Xuelei; Retnoningrum, Debbie S.; Dijkstra, Bauke W.; Tjandrawinata, Raymond R.; Rachmawati, Heni

Published in:
International Journal of Biological Macromolecules

DOI:
10.1016/j.ijbiomac.2017.04.014

Publication date:
2017

Acta Materialia 129 (2017) 1–10

Contents lists available at ScienceDirect

Acta Materialia

journal homepage: www.elsevier.com/locate/actamat

Full length article

Size effect on deformation twinning in face-centred cubic single crystals: Experiments and modelling

Z.Y. Liang [a, b], J.T.M. De Hosson [c], M.X. Huang [a, b, *]

[a] Department of Mechanical Engineering, The University of Hong Kong, Hong Kong, China
[b] Shenzhen Institute of Research and Innovation, The University of Hong Kong, Shenzhen, China
[c] Department of Applied Physics, Zernike Institute for Advanced Materials, University of Groningen, Groningen, The Netherlands

ARTICLE INFO

Article history:
Received 24 August 2016
Received in revised form
30 January 2017
Accepted 22 February 2017
Available online 23 February 2017

Keywords:
Deformation twinning
Size effect
Radiation
TWIP steel
Pillar

ABSTRACT

In addition to slip by dislocation glide, deformation twinning in small-sized metallic crystals also exhibits size effect, namely the twinning stress increases with decreasing sample size. In order to understand the underpinning mechanisms responsible for such effect, systematic experiments were carried out on the small-sized single-crystalline pillars of a twinning-induced plasticity steel with a face-centred cubic structure. The flow stress increases considerably with decreasing pillar diameter from 3 to 0.5 μm, demonstrating a substantial size effect with a power exponent of 0.43. Detailed microstructural characterization reveals that the plastic deformation of the present pillars is dominant by twinning, primarily via twin growth, indicating that the size effect should be related to deformation twinning instead of slip by dislocation glide. Subsequent modelling works indicate that twinning can be accomplished by the dissociation of the ion-radiation-induced vacancy Frank loops in the damaged subsurface layer of the pillars, and the size effect is attributed to the ion-radiation-induced compressive stress in the subsurface layer, which decreases with pillar diameter.

1. Introduction

Deformation twinning is one of the plastic deformation mechanisms in crystalline materials. It has been found in face-centred cubic (FCC), body-centred cubic (BCC), hexagonal-close-packed (HCP) and lower symmetry metals and alloys [1–5]. For many years, deformation twinning has been considered as a supplementary deformation mechanism when dislocation glide is restricted due to limited slip systems or certain extreme deformation conditions such as high-strain rate during shock loading and low temperature [4–6]. In some cases, only a limited amount of twins are formed during plastic deformation and their contribution to the total plastic strain is less significant [4,5]. Nonetheless, in recent years, deformation twinning has become increasingly important as intense twinning phenomenon is discovered in plastic deformation of certain structural engineering metals and alloys, such as austenitic steels [7–9], Mg [10,11] and Ti [12,13] alloys, high entropy alloys [14–16] and shape memory alloys [17]. A substantial amount of deformation twins with a twin volume fraction up to around 0.2 can be formed during plastic deformation of these materials [18]. With elegant arrays of deformation twins formed within the grains, these materials generally exhibit an enhanced work-hardening rate and thereby excellent combination of high strength and good ductility [12,19,20]. In literature, such twinning effect has been commonly referred as the twinning-induced plasticity (TWIP) effect. In addition, the formation of twins can also improve the fracture toughness [21] and the damage tolerance during cyclic loading [22]. In short, deformation twinning has become as an important deformation mechanism as dislocation glide and martensitic transformation.

In recent years, the deformation behaviour of nanometre- and micrometre-sized metallic crystals has attracted considerable interest due to the increasing use of nano- and micro-electromechanical systems (NEMS/MEMS) in the microelectronics industry [23–25]. The most remarkable discovery for the small-scale plasticity is the size effect, namely, the flow stress of a crystal depends largely on its geometrical dimensions [23,25–27]. In the past decade, research on the size effect phenomenon has been generally focused on the unusual dislocation behaviour in confined dimensions. In comparison, the twinning behaviour in small-sized

* Corresponding author. Department of Mechanical Engineering, The University of Hong Kong, Hong Kong, China.
E-mail address: mxhuang@hku.hk (M.X. Huang).

http://dx.doi.org/10.1016/j.actamat.2017.02.063
1359-6454/

metallic crystals has received much less attention. By performing compression experiments on single-crystalline pillars of a Ti alloy, Yu et al. [28] demonstrated for the first time that the stress for twinning initiation increases dramatically with the pillar diameter decreased from 8 to 1 μm. They proposed that certain dislocations with a particular configuration should be the necessary 'promoters' for twinning and the increase of the critical twinning stress should be due to greater difficulty in finding such promoters in a smaller sample. While this model can reproduce the size effect on critical twinning stress observed in the experiments, no evidence was provided to prove the effectiveness of the proposed twinning mechanism. Ye et al. [29] extended the sample size down to the submicron-scale and also found size effect on the critical twinning stress in their single-crystalline pillars of Mg and its alloy. For FCC metals, it was reported by Seo et al. [30] that the stress for both twin nucleation and twin growth also increases with smaller diameter of Au single-crystalline nanowires. Considering that the diameter varies between 250 and 40 nm, which is down to the nanometre-scale, the size effect on twin growth via the propagation of the coherent twin boundary has been attributed to the enhanced surface effect due to larger surface-to-volume ratio in a smaller sample. Yet, no explanation was provided for the size effect on twin nucleation. In addition to size effect, deformation twinning in small-sized FCC metals is found to follow a different twinning mechanism compared to their bulk counterparts, i.e. twinning is accomplished by emission of Shockley partial dislocations (SPDs) on successive {111} planes from surface [31–36]. This mechanism is captured in extensive molecule dynamics (MD) simulations on the deformation behaviour of nanometre-sized FCC single crystals [37–42] and is directly proved by the in-situ tensile experiments on Au single-crystalline nanowires [43]. Based on this mechanism, a physically-based model has been developed previously by Liang and Huang [44], which can quantitatively predict the stress-strain relation and the corresponding twin evolution during plastic deformation of small-sized FCC single crystals. The model is able to reproduce the experimental twin evolution in terms of the total twin formation, the twin morphology and the occurrence of twinning burst.

In the present work, systematic experiments were conduct on the single-crystalline pillars of a TWIP steel with a diameter from 3 to 0.5 μm in order to investigate the size effect on deformation twinning in small-sized FCC single crystals. It will be shown that the twinning stress increases considerably at decreasing pillar size, demonstrating a substantial size effect. In addition, modelling works will be carried out to demonstrate that the ion-radiation-induced vacancy Frank loops in the damaged subsurface layer can be the sources for twinning and the ion-radiation-induced compressive stress in the damaged subsurface layer should be the reason for the size effect on twinning stress observed in experiments.

2. Experiments

A TWIP steel with a chemical composition of Fe-22Mn-0.6C (wt.%) and a low stacking fault energy of 21.8 mJ m^{-2} [45] was employed as the experimental carrier. This material is ideal for studying deformation twinning in FCC structure since it has a fully austenitic microstructure and it is willing to twin during plastic deformation at ambient temperature. This TWIP steel was first subjected to a cold rolling with a thickness reduction of 70%. A sample with dimensions of $10 \times 10 \times 1$ mm^3 was cut from the cold-rolled sheet and then annealed at 1273 K for an hour in order to obtain a fully-recrystallized microstructure with a large grain size. After mechanical grinding and polishing down to 50 nm, the sample was put into a LEO 1530 FEG scanning electron microscopy (SEM) operated at 20 kV for an electron backscatter diffraction (EBSD) mapping. Large grains with the [001] orientation normal to the sample surface were selected as the target grains for fabricating the single-crystalline pillars. A FEI Quanta 200 3D Dual-Beam focus ion beam (FIB) was used to fabricate single-crystalline pillars with diameters of 3, 1 and 0.5 μm within the selected grains. Hereafter, the pillars with diameters of 3, 1 and 0.5 μm are named as the D3, D1 and D0.5 pillars, respectively. The milling currents ranged from 20 nA for coarse milling to 50 or 10 pA for surface polishing. Three pillars were made for each diameter. The aspect ratio is between 2.5:1 and 4:1 and the taper angle is within 5°. An Agilent G200 nanoindentation equipped with a flat punch was utilized to compress the D3 and D1 pillars. For the D0.5 pillars, the compression experiments were carried out in a Hysitron PI 85 picoindenter in order to ensure the accuracy in load measurement with highly sensitive transducer assembly. All the compression experiments in both devices were conducted in load-controlled mode at ambient temperature. Transmission electron microscopy (TEM) samples were sliced from the compressed pillars along the loading axis and then further thinned down to 100 nm with FIB. Detailed TEM characterization was carried out in an FEI Tecnai G2 20 scanning transmission electron microscopy (STEM) equipped with an energy-dispersive X-ray spectroscopy (EDS) operated at 200 kV.

3. Experimental results and discussion

3.1. Deformation behaviour under compression

The engineering stress-strain curves of the D3, D1 and D0.5 pillars under compression are shown in Fig. 1(a). Here, the engineering stress is calculated with the area of cross section at the mid-height and the engineering strain is the normal strain along the pillar axis. The flow stress increases considerably with the pillar diameter decreased from 3 to 0.5 μm, demonstrating a substantial size effect. In particular, the average yield stress of the D3, D1 and D0.5 pillars, which is determined as the stress for inducing the first strain burst with a size (i.e. the strain magnitude) larger than 0.5%, is 302 ± 52, 490 ± 46 and 671 ± 50 MPa, respectively. The reported critical shear stresses for deformation twinning and dislocation slip in both bulk and small-sized single crystals of TWIP steels are summarized in Section 1 of Supplementary materials for comparison. As shown in Fig. 1(b), the relation between the yield stress (σ_y) and the diameter (D) was fitted with a power law equation ($\sigma_y = A \cdot D^{-n}$, delineated by the dash line), which leads to a power law exponent of 0.43. After yielding, all the stress-strain curves exhibit jerky plastic flow (as shown in Fig. 1(a)) and three typical examples (one for each pillar size) are replotted in Fig. 1(c) in order to show the details. The plastic deformation proceeds by discrete strain bursts at relatively constant flow stress and the strain rate of the strain bursts varies largely from 0.01 to 0.91 s^{-1}. Between the strain bursts, the pillars mainly deform elastically with a modulus similar to that of the initial elastic loading before yielding. The strain bursts including the size (0.5% is set as the size limit for measurement) and the stress are measured from all the stress-strain curves in Fig. 1(a) and summarized in Fig. 1(d). With the diameter reduced from 3 to 0.5 μm, the stress of the strain bursts with similar size increases and meanwhile the size becomes much more scattered, from the range of 0.7–4.9% for the D3 pillars to the range of 0.5–9.1% for the D0.5 pillars.

After compression, SEM characterization was carried out to observe the appearance of all the deformed pillars and three typical examples (one for each pillar size) are presented in Fig. 2 with their stress-strain curves shown in Fig. 1(c). The most distinct feature of all the deformed pillars is the smooth inclined surface and one typical example is marked by the solid arrow in Fig. 2(b). For the

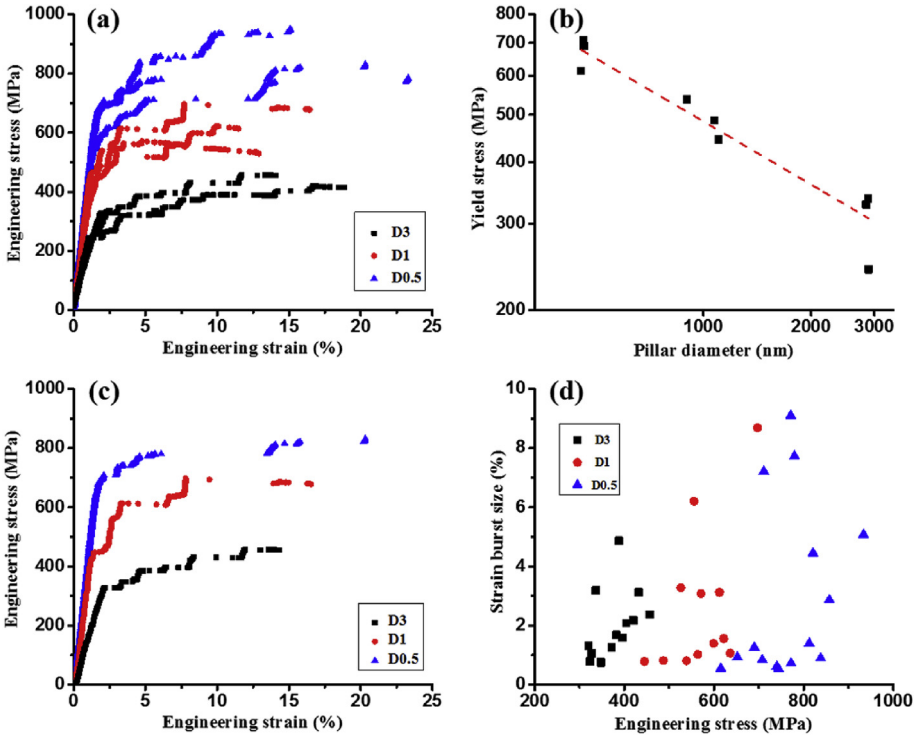

Fig. 1. (a) The engineering stress-strain curves of the D3, D1 and D0.5 pillars under compression; (b) the relation between the yield stress and the diameter, which was fitted by a power law as delineated by the dash line; (c) Selected stress-strain curves (one for each pillar size) from (a); (d) the strain bursts with the size and the stress measured from all the stress-strain curves in (a).

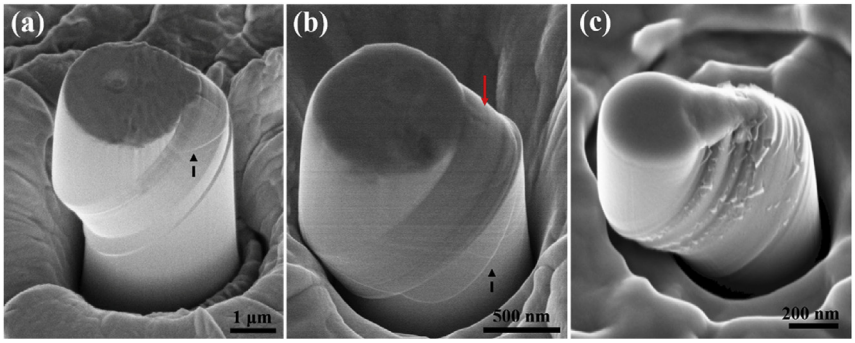

Fig. 2. SEM images of the (a) D3, (b) D1 and (c) D0.5 pillars after compression.

small-sized pillars deforming by dislocation glide, surface steps are commonly observed on the pillar surface, which should be formed via repeated dislocation glides on the same slip plane [46,47] (one typical example is shown in Section 2 of Supplementary materials). The absence of such surface steps on the present deformed pillars indicates that plasticity should not be dominated by dislocation glide. In addition, the inclined surface also demonstrates that shear deformation mainly proceeds on one primary set of slip planes, regardless of the fact that multiple slip should be favoured for compression along the [001] orientation. Still, a second set of slip planes is also activated in certain pillars as indicated by the slip trances on the pillar surface (marked by the dash arrows in Fig. 2(a) and (b)).

3.2. Microstructure after compression

TEM characterization was conducted to examine the microstructure of the deformed pillars. Fig. 3(a), (b) and (c) are the respective TEM images of the D3, D1 and D0.5 pillars shown in Fig. 2. Banded structures with various thickness (dark contrast in Fig. 3(a) and (b) and bright contrast in Fig. 3(c)) can be observed in all these pillars. Selected area diffraction observations were carried out at the boundaries of these bands and the diffraction patterns for the D3, D1 and D0.5 pillars are displayed in Fig. (d), (e) and (f), respectively. These diffraction patterns prove that these bands are deformation twins (the subscripts '*M*' and '*T*' represent matrix and twin, respectively) and the twins within one pillar follow the same $(111)[11\bar{2}]$ twinning system. By comparing the twin morphology in Fig. 3 to the corresponding appearance of deformed pillars in Fig. 2, it is found that there is a one-to-one relation between the deformation twin inside the pillar and the smooth inclined surface. Similar one-to-one relation has also been found in the pillars with ε-martensitic transformation during plastic deformation [48]. Yet, the angle between the inclined surface and the original pillar

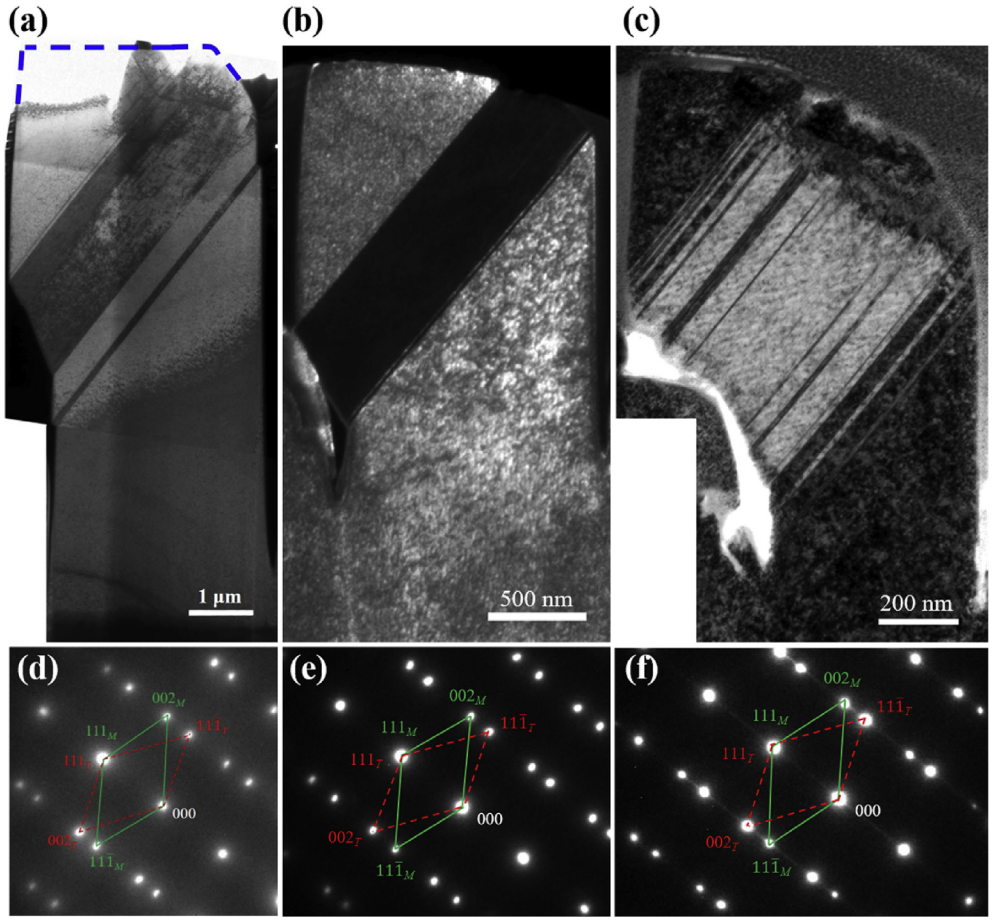

Fig. 3. TEM images of the (a) D3, (b) D1 and (c) D0.5 pillars after compression with their selected area diffraction patterns shown in (d), (e) and (f), respectively.

surface for deformation twin is larger than that for ε-martensite. For an FCC single-crystalline pillar compressed along the [001] orientation, the angle between the inclined surface and the original pillar surface is 35.26° for deformation twins while it is 15.79° for ε-martensites. As dislocation glide, deformation twinning and ε-martensitic transformation induce distinct surface features, it is feasible to evaluate the active deformation mechanism based on the appearance of the deformed pillar. By applying this method to all the present pillars, it is found that the plastic deformation should be dominated by deformation twinning, consistent with the previous findings in the micro-pillars of the same TWIP steel. Such phenomenon has also been reported in Au single-crystalline nanowires, the plasticity of which is completely accommodated by the nucleation and growth of one single twin [43]. Nevertheless, there should be certain amount of dislocation activities during the compression of the present pillars, which is based on pre-existing dislocations inside the samples, yet their contribution to plasticity should be insignificant due to a two-fold reason. Firstly, the number of pre-existing dislocations inside the pillar is limited considering the relatively low initial dislocation density of the recrystallized bulk sample and the small volume of pillars that sampled from this bulk sample. Moreover, dislocations within such small volume, as commonly reported in literature, can easily annihilate at pillar surface, resulting in suppression of dislocation multiplication [25,49].

In order to quantitatively characterize the twin structure, the thickness of all the twins in the pillars shown in Fig. 3 was measured at the edge-on direction in TEM. The twins with a thickness smaller than 10 nm were not considered in the analysis due to the limit of resolving power of the present TEM measurement. The total twin thickness (T_{tot}), the respective numbers of the large (N_l) and small (N_s) twins (the twin thickness equal to 10% of the diameter is chosen as the demarcation line for each pillar size), and the ratio of the total twin thickness contributed by the large twins (P_t) are summarized in Table 1. Regardless of a large total twin thickness, a limited number of twins are formed and the large twins account for most of the total twin thickness. Such twin structure indicates that twin growth instead of twin nucleation should be favoured during plastic deformation of all the present pillars with different diameters.

3.3. Size effect on twinning stress

It has been pointed out that the unusual size-dependent strength discovered in various FCC metals including Al, Ni, Cu, Au and Ag with a wide range of sample size from several tens of micrometres down to several tens of nanometres can be described by a universal power law [50–52]. As the plasticity of these FCC

Table 1
Twin structure in the deformed pillars with different diameter.

#	T_{tot} (nm)	N_l	N_s	P_t (%)
D3	1650	1	1	94.2
D1	517	1	1	96.5
D0.5	515	4	6	80.8

metals is completely accommodated by dislocation glide, the size effect is attributed to the constraint of sample dimensions on dislocation glide, which has been explained by the single-arm source theory in the micron-scale [53–55] and the dislocation starvation theory in the nanometre-scale [49,56–58]. In short, the size effect discovered in these FCC metals is related to dislocation nucleation and mean free path of dislocation glide. By reviewing the experimental results in poly- and single-crystalline metallic thin films and small-sized structures, Kraft et al. [23] reasoned that the size dependency should be separated into three regimes with different power law exponents depending on the operating plasticity mechanisms. With decreasing sample dimensions, there is a transition in the dominant plasticity mechanism from collective dislocation dynamics inside the crystals to surface dislocation nucleation. This transition is supported by experiments [59,60] and MD simulations [61,62] which further reveal that the surface dislocation nucleation is not as sensitive as collective dislocation dynamics to the sample size, resulting in a smaller power exponent compared to that of collective dislocation dynamics normally between 0.6 and 0.7 [50].

In the present work, substantial size effect on flow stress has been observed in the single-crystalline pillars of a TWIP steel with a diameter ranging from 3 to 0.5 μm and this size effect should be related to deformation twinning (in terms of both twin nucleation and twin growth) instead of dislocation glide. Considering that twinning is accomplished by surface dislocation emission, the size effect on the twinning stress should have a power law exponent smaller than the range of 0.6–0.7 for collective dislocation dynamics, consistent with the experiments as 0.43 was obtained in the present pillars (shown in Fig. 1(b)). Size effect on twinning stress has also been found in Au single-crystalline nanowires with diameters varying from 40 to 250 nm [30]. As this sample size enters the nanometre-scale, such size effect has been attributed to a more significant effect of surface energy on the plastic deformation due to a higher surface-to-volume ratio in smaller samples. Yet, the diameter of the present pillars is in the micrometre- and submicron-scale, which should not have a substantial surface-to-volume ratio. Therefore, the size effect on twinning stress discovered in the present pillars should be explained by an alternative mechanism.

3.4. Mechanism for emission of SPDs

In order to reveal the underlying physics of the size effect on twinning, the mechanism for twinning should be understood. As demonstrated by extensive experiments [43,61,63] and MD simulations [37–42], the essential process for deformation twinning in small-sized FCC metals is the emission of SPDs from free surface. According to the MD simulations [40–42], SPDs can nucleate from free surface at an ultrahigh stress generally approaching the theoretical limit. The experiments on the small-sized defect-scarce metallic crystals, e.g. micro-whiskers, prove the necessity of such ultrahigh stress [59,64,65]. However, the emission of SPDs from free surface occurs at a much lower stress than the theoretical limit in all the present pillars as shown in Fig. 1(a), indicating that an alternative mechanism instead of surface nucleation should be responsible for emission of SPDs. Based on the experiments on Mo single-crystalline micro-pillars, Shim et al. [66] demonstrated that the ion radiation during FIB milling can substantially decrease the sample strength. While the pristine pillars without ion radiation exhibit a yield stress of around 9 GPa, the ones with their surfaces subjected to ion milling display a much lower yield stress of around 1 GPa. Detailed TEM characterization of the samples subjected to ion radiation reveals that the ion bombardment will damage the sample surface to certain depth and may induce various defects such as an amorphous layer, dislocation loops and ion precipitates into the damaged subsurface layer [67–70]. By performing in-situ TEM compression experiments, Lee et al. [71] demonstrated that the ion-radiation-induced dislocation loops with a radius of several tens of nanometres in the damaged subsurface layer can expand at a stress much lower than the theoretical limit. This phenomenon indicates that the ion-radiation-induced dislocations in the damaged subsurface layer can act as alternative dislocation sources when there is a limited number of dislocation sources inside the sample to accommodate the plastic deformation. Ion-radiation-induced dislocations can also be found in the present TWIP steel. Fig. 4(a) displays the microstructure of the as-received recrystallized TWIP steel sample before FIB ion radiation. The dislocation density, estimated by applying the line cutting method (totally 37 lines) to the TEM images obtained in various locations, is $1.46 \pm 0.63 \times 10^{13}$ m^{-2}. After a routine FIB milling process, the dislocation density increases dramatically, which is roughly estimated to be around 1.2×10^{15} m^{-2} as shown in Fig. 4(b). These radiation-induced dislocations observed in the present TWIP steel pillars should be vacancy Frank loops instead of perfect loops observed in the Al pillars [71] due to the difference in stacking fault energy (a detailed discussion can be found in Section 3 of Supplementary materials). In order to reduce the self-energy, the vacancy Frank loop on certain {111} plane usually develops a hexagonal shape with the six sides aligned along the three ⟨110⟩ orientations of this {111} plane [72]. Driven by the stress, the dislocation segment of one side may dissociate into a SPD gliding on a conjugate {111} plane and a sessile stair-rod dislocation with an intrinsic stacking fault connecting between them. The dislocation reaction of this dissociation can be:

$$\frac{1}{3}\left[11\bar{1}\right]_{(11\bar{1})} \rightarrow \frac{1}{6}\left[11\bar{2}\right]_{(111)} + \frac{1}{6}[110]_{sessile} \tag{1}$$

i.e. $\alpha A \rightarrow \delta A + \alpha\delta$. Such dislocation dissociation is energy favourable since the total dislocation line energy can be reduced ($b_{\alpha A}^2 > b_{\delta A}^2 + b_{\alpha\delta}^2$) and subsequently balanced by the increasing faulting energy, similar to the situation, where a perfect dislocation dissociates into two SPDs and a ribbon of intrinsic stacking fault between them in FCC metals with low stacking fault energy. In literature, this dissociation of Frank dislocation has been used to explain the formation of the stacking fault tetrahedron from a vacancy Frank loop [73], which has also been captured by MD simulations [74–76]. For the present TWIP steel pillars, such dissociation of radiation-induced vacancy Frank loops in the damaged subsurface layer may be the mechanism for the emission of SPDs and the resultant formation of deformation twins. It should be noticed that certain amount of interstitial Frank loops should also exist in the damaged subsurface layer, yet they are difficult to dissociate into SPDs since the required dislocation reaction:

$$\frac{1}{3}\left[\bar{1}\bar{1}1\right]_{(11\bar{1})} \rightarrow \frac{1}{6}\left[11\bar{2}\right]_{(111)} + \frac{1}{6}\left[\bar{3}\bar{3}4\right]_{\text{sessile}} \tag{2}$$

or

$$\frac{1}{3}\left[\bar{1}\bar{1}1\right]_{(11\bar{1})} \rightarrow \frac{1}{6}\left[1\bar{2}1\right]_{(111)} + \frac{1}{6}\left[\bar{3}01\right]_{sessile} \tag{3}$$

increases the total dislocation line energy and is therefore not energy favourable. In this case, the interstitial Frank loops are not considered as the sources for emission of SPDs.

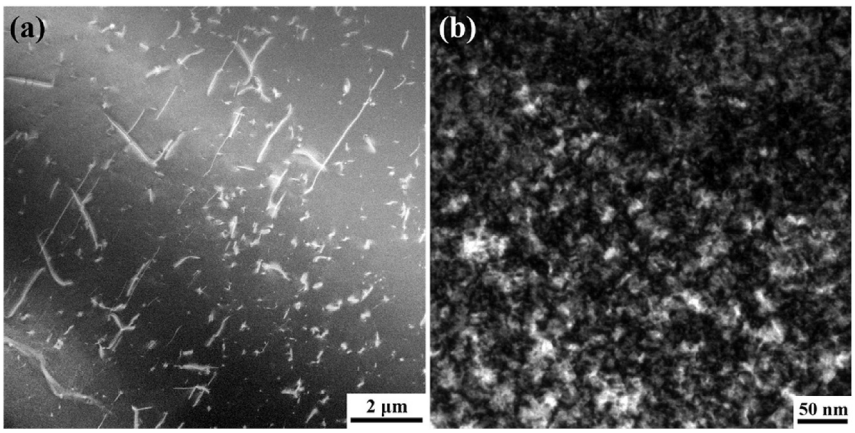

Fig. 4. (a) A STEM dark field image showing the initial dislocation structure of the present TWIP steel sample before ion radiation; (b) a TEM bright field image of the dislocation structure after ion radiation.

4. Modelling and discussion

4.1. Critical stress for the dissociation of a vacancy Frank loop

The critical stress for the dissociation of a vacancy Frank loop will be determined in order to evaluate the effectiveness of this mechanism for emission of SPDs in the present pillars. The dislocation configuration adopted for calculation is illustrated in Fig. 5(a). A vacancy Frank loop in a hexagonal shape lies in a $(11\bar{1})$ plane with an intrinsic stacking fault (marked in grey in Fig. 5(a)) inside. Driven by a resolved shear stress along the twinning direction $[11\bar{2}]$, a segment of the Frank loop ($b_{\alpha A} = \frac{1}{3}[11\bar{1}]$) may dissociate into a SPD ($b_{\delta A} = \frac{1}{6}[11\bar{2}]$ and marked as the green line in Fig. 5(a)) and a sessile stair-rod dislocation ($b_{\alpha\delta} = \frac{1}{6}[110]$ and marked as the blue line in Fig. 5(a)). The subsequent gliding of SPD on the conjugate (111) plane, which is not bounded by stacking faults or twin boundaries) leads to the formation of an intrinsic stacking fault (also marked in grey in Fig. 5(a)), which can be considered as the nucleation of a twin precursor (Mode I). The energy change during the dissociation of the vacancy Frank loop and the subsequent expansion of SPD ($\Delta G_{d,l}$) should include the contributions from the dislocation line energy (including $Q_{line,\alpha A}$, $Q_{line,\alpha\delta}$ and $Q_{line,\delta A}$ for the Frank dislocation, stair-rod dislocation and SPD, respectively), the faulting energy (Q_{sf}), the work done by

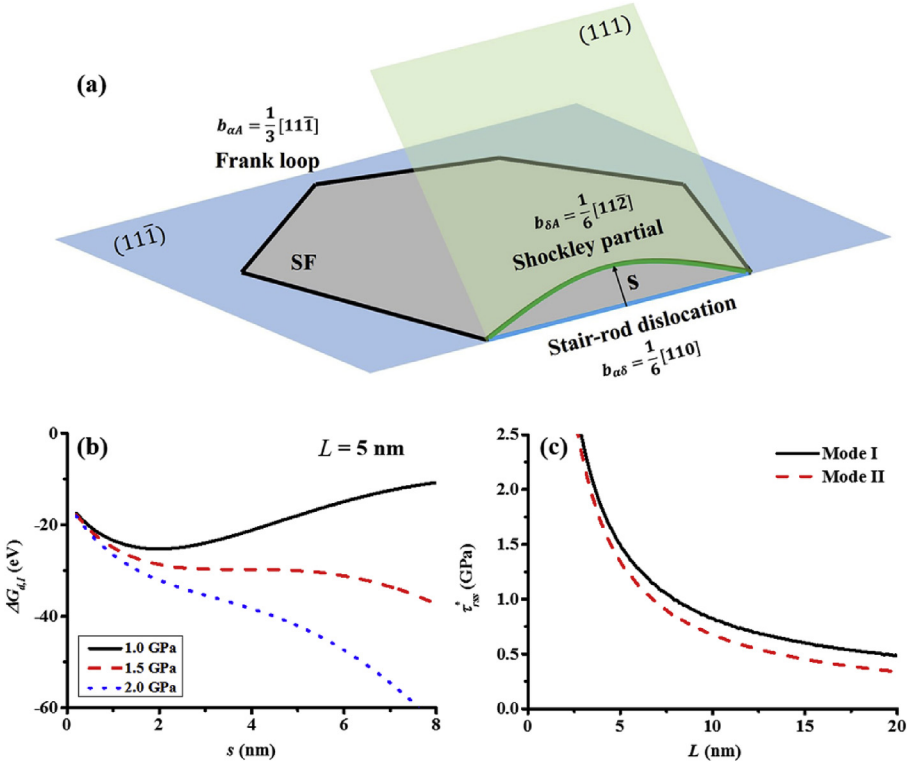

Fig. 5. (a) Schematic for dissociation of a vacancy Frank loop; (b) the evolution of energy change with the dissociation distance at different resolved shear stress in Mode I for a Frank dislocation segment with a length of 5 nm; (c) the relation between the length of the Frank dislocation segment and the critical resolved shear stress for dissociation in Mode I and II.

the applied stress (Q_{work}) and the interaction energy between SPD and the stair-rod dislocation (Q_{inter}) as:

$$\Delta G_{d,I} = -Q_{line,\alpha A} + Q_{line,\alpha\delta} + Q_{line,\delta A} + Q_{sf} - Q_{work} - Q_{\mathrm{inter}} \quad (4)$$

The detailed formulation for each energy component can be found in Section 4 of Supplementary materials. In general, the energy change is a function of the dissociation distance (s, delineated by the arrow in Fig. 5(a)), the length of the Frank dislocation segment (L) and the resolved shear stress (τ_{rss}). Fig. 5(b) displays the evolution of energy change with the dissociation distance at different resolved shear stress in Mode I for a 5 nm Frank dislocation segment. At a sufficiently high resolved shear stress, the energy change becomes a monotonic decreasing function of the dissociation distance, indicating that dissociation can occur spontaneously without any energy barrier. For a Frank dislocation segment with a given length, the critical resolved shear stress (τ^*_{rss}) for dissociation refers to the one when maximum derivative of the energy change is equal to zero. Accordingly, the relation between the length of the Frank dislocation segment and the critical resolved shear stress for dissociation in Model I is summarized in Fig. 5(b).

In addition to Mode I, the dissociation of a Frank dislocation segment can also occur at the neighbour {111} planes of stacking faults (either intrinsic or extrinsic) or twin boundaries (Mode II). For FCC metals, it is demonstrated by experiments and *ab initio* calculations that intrinsic stacking fault energy (γ_{isf}), extrinsic stacking fault energy (γ_{esf}) and twin boundary energy (γ_t) generally follow a relation $\gamma_{sf} \approx \gamma_{esf} \approx 2\gamma_t$ [77]. Accordingly, no additional faulting energy should be induced when the dissociation occurs in Mode II. In this condition, the free energy change ($\Delta G_{d,II}$) during dissociation is revised as:

$$\Delta G_{d,I} = -Q_{line,\alpha A} + Q_{line,\alpha\delta} + Q_{line,\delta A} - Q_{work} - Q_{\mathrm{inter}} \quad (5)$$

The evolution of the energy change with the dissociation distance in Mode II shares a similar feature to that in Mode I, i.e. the energy change becomes a monotonic decreasing function of the dissociation distance when the resolved shear stress is higher than certain critical value. The relation between the length of Frank dislocation segment and the critical resolved shear stress for dissociation in Mode II is also summarized in Fig. 5(b).

The critical resolved shear stresses for dissociation in both Mode I and II decrease quickly with increasing length of the Frank dislocation segment. For the same length, the critical stress in Mode II is smaller than that in Mode I. In this condition, the dissociation is normally organized in a way that once intrinsic stacking faults are formed in Mode I, the subsequent dissociations tend to occur successively in Mode II on the neighbour {111} planes, transforming these intrinsic stacking faults in sequence into extrinsic stacking faults, then twins and further twin thickening as twin growth. Accordingly, twin growth in Mode II is favourable instead of twin nucleation in Mode I, in consistent with the experimental observations as shown in Fig. 3. In literature, it is reported that the diameter of the ion-radiation-induced Frank loops is relatively small, normally within tens of nanometres, compared to those induced by neutron radiation, due to the limited penetration depth of energetic ions [68,71,78]. As shown in Fig. 4(b), the Frank loops formed in the present pillars also exhibit a similar size range and therefore the side length of the hexagonal-shaped loops should be at maximum around 10 nm since $L = d/2$, where d is the diagonal of the loops within tens of nanometres. The minimum critical resolved shear stress for dissociation of the largest Frank loop in Mode I, according to the Fig. 5(b), is 825 MPa, which is also the critical stress for twin nucleation. Yet, the yield stress at which twinning initiates in the present pillars, is between 242 and 708 MPa as shown in Fig. 1(a), corresponding to a resolved shear stress between 114 and 333 MPa with a Schmid factor of 0.471 for the active twinning system $(111)[11\bar{2}]$. The gap on the critical stresses for the twinning initiation between experiments and modelling can be explained by the pre-existing internal stress in the damaged subsurface layer, which facilitates the dissociation of vacancy Frank loops.

4.2. Ion-radiation-induced compressive stress in the damaged subsurface layer

In literature, it is frequently reported that ion radiation can induce permanent deformation of nanometre-sized crystals, e.g. nanowires, which is commonly known as the ion beam-induced bending [79–82]. This phenomenon has been attributed to the ion-radiation-induced defects such as point defects and implanted ions, both of which can cause local volume change, i.e. swelling, in the damaged subsurface layer and may induce substantial internal stress into this layer due to the constraint from surrounding materials without radiation effects [82–84]. The ion-radiation-induced internal stress should also exist in the damaged subsurface layer of the present pillars and may facilitate the dissociation of vacancy Frank loops for twinning. In order to quantitatively evaluate this ion-radiation-induced internal stress, a physical model was developed, which is able to predict the thickness of the damaged subsurface layer, the concentrations of point defects and implanted ions and the resultant volume change (the details of the model can be found in Section 5 of Supplementary materials). Based on the model, the simulation on the radiation effects was carried out in Fe irradiated with 30 kV Ga ion at 293 K to demonstrate as an example. Fig. 6(a) displays the concentrations of vacancies and implanted Ga atoms in lattice positions as functions of depth in the damaged subsurface layer. The maximum depth of lattice Ga atoms, which corresponds to the penetration depth of Ga ions, is around 30 nm, in consistent with the value determined by EDS line scan across the free surface of a D3 pillar (details in Section 6 of Supplementary materials). As vacancies cause contraction and lattice Ga atoms induce expansion due to a larger atomic radius than Fe (the self-interstitial atoms and interstitial Ga atoms are not considered due to their minor concentrations), their combined effects lead to a volume expansion of a few percent in the damaged subsurface layer shown in Fig. 6(b). Yet, this expansion should be constraint by the pillar core without ion radiation, which results in a pre-existing compressive stress in the damaged subsurface layer and a tensile stress in the pillar core before compression experiments. Supposed the volume expansion of the damaged subsurface layer is fully constraint without any geometrical change, the maximum strain ($\varepsilon_{i,\max}$) along the pillar axis, should be $\varepsilon_{i,\max} = P_{\max}/3 = 0.9$ % (where $P_{\max}$ is the maximum volume expansion of 2.7% as identified in Fig. 6(b)). Accordingly, the maximum compressive stress ($\sigma_{i,\max}$) along the pillar axis in the damaged subsurface layer can be estimated as $\sigma_{i,\max} = E \cdot \varepsilon_{i,\max} = 1.6\ GPa$ (where E is the Young's modulus equal to 172.9 GPa). Such high ion-radiation-induced internal stress has also been reported in other miniature crystals, which is normally in the order of several GPa [80,82,85]. As captured by the model, the ion radiation effects depend largely on the accelerating voltage and the types of ion and target material, yet marginally on the irradiation dose, which should be due to the limited penetration depth of energetic ions. Therefore, the pillars with different diameter, which are all fabricated by FIB milling with 30 kV Ga ions, should contain similar radiation damage. In other words, the thickness of the damaged subsurface layer, the defect concentration and the associated volume change should be similar in pillars with different diameter.

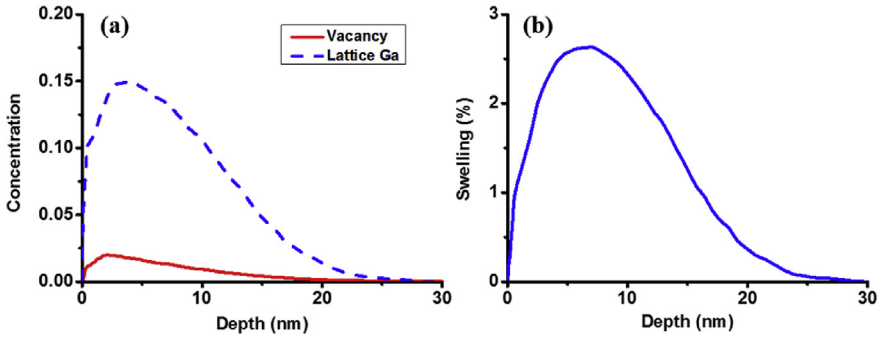

Fig. 6. (a) Concentrations of vacancies and lattice Ga atoms; (b) the resultant swelling as a function of depth.

4.3. Size effect due to the pre-existing compressive stress in the damaged subsurface layer

In order to evaluate the effect of the pre-existing compressive stress on twin nucleation via dissociation of vacancy Frank loops in Mode I in the damaged subsurface layer, a composite model was proposed by considering the interaction between the damaged subsurface layer and the unaffected pillar core. After ion radiation during FIB milling, the damaged subsurface layer, at the absence of constraint, should undertake an expansion with an assumed homogeneous swelling of P and the corresponding dimensional change along the pillar axis should be $P/3$. Yet, this dimensional change will be constraint by the pillar core and force equilibrium between the damaged subsurface layer and pillar core leads to a pre-existing compressive stress ($\sigma_{i,s}$) in the damaged subsurface layer and a tensile stress ($\sigma_{i,c}$) in the pillar core as illustrated by the transverse section of a pillar shown in Fig. 7(a). The force equilibrium is

$$\sigma_{i,s}\cdot\frac{\pi}{4}\left[D^2-(D-2t)^2\right]=\sigma_{i,c}\cdot\frac{\pi}{4}(D-2t)^2 \tag{6}$$

where t is the thickness of the damaged subsurface layer as marked in Fig. 7(a) and

$$\sigma_{i,s}=E\cdot\left(\frac{P}{3}-\frac{\Delta H}{H_0}\right) \tag{7}$$

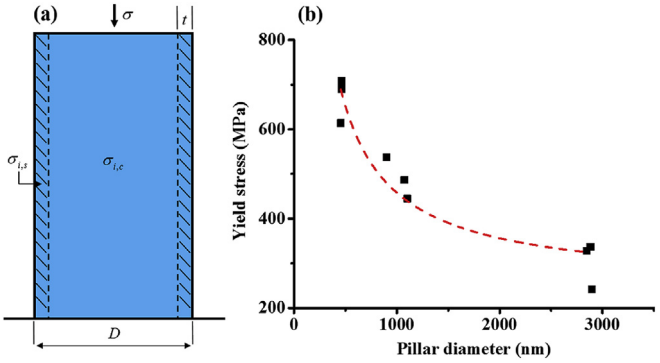

Fig. 7. (a) Schematic for the composite model used to evaluate the effect of the pre-existing internal stress on the yield stress of pillars with different diameter; (b) the relation between the yield stress and the pillar diameter, which is fitted by the composite model as delineated by the dash line.

$$\sigma_{i,c}=E\cdot\frac{\Delta H}{H} \tag{8}$$

where $\Delta H/H_0$ is the dimensional change along the pillar axis of both the damaged subsurface layer and the pillar core when the force equilibrium is achieved after radiation. The combination of Eqs. (6)–(8) leads to:

$$\sigma_{i,s}=E\cdot\frac{P}{3}\cdot\left(1-\frac{2t}{D}\right)^2 \tag{9}$$

Under an external stress of σ, both the damaged subsurface layer and the pillar core undertake the same elastic strain of ε with a force equilibrium as:

$$(\sigma_{i,s}+\varepsilon E)\cdot\frac{\pi}{4}\left[D^2-(D-2t)^2\right]+(\varepsilon E-\sigma_{i,c})\cdot\frac{\pi}{4}(D-2t)^2=\sigma\cdot\frac{\pi}{4}D^2 \tag{10}$$

Accordingly, the stress built up in the damaged subsurface layer (σ_{surf}) should be:

$$\sigma_{surf}=\sigma+\sigma_{i,s}=\sigma+E\cdot\frac{P}{3}\cdot\left(1-\frac{2t}{D}\right)^2 \tag{11}$$

When the stress in the damaged subsurface layer is equal to the critical stress for twinning via dissociation of vacancy Frank loops (σ_{crit}) in Mode I, the pillar should yield via twinning:

$$\sigma_y=\sigma_{crit}-E\cdot\frac{P}{3}\cdot\left(1-\frac{2t}{D}\right)^2 \tag{12}$$

As discussed in Section 4.2, the thickness of the damaged subsurface layer, the concentration of various defects and the associated volume expansion are similar in pillars with different diameter. Therefore, P and $t=30$ nm should be the same for pillars with different diameter. The σ_{crit} which depends on the size of vacancy Frank loops should also be similar in pillars with different diameter due to similar defect concentrations. In this case, the yield stress depends only on the diameter. By fitting the experimental relation between the yield stress and the pillar diameter with Eq. (12), as delineated by the dash line in Fig. 7(b), σ_{crit} and P are determined to be 2029 MPa and 3%, respectively. The pre-existing compressive stresses in the damaged subsurface layers of the D3, D1 and D0.5 pillars, according to Eq. (9), are 1708, 1571 and 1377 MPa, respectively, which are reasonably high compared to the values reported in literature [80,82,85] and are consistent with the estimation discussed in Section 4.2. Besides, the critical stress for twin nucleation via dissociation of vacancy Frank loops in Mode I is 956 MPa in shear stress, also consistent with the prediction as

discussed in Section 4.1. In short, the size effect on the critical twinning stress should be attributed to the ion-radiation-induced compressive stress in the damaged subsurface layer, which decreases with pillar diameter. It should be noticed that such size effect is based on surface dominant plasticity mechanism such as the Frank loop dissociation in the present pillars since significant ion-radiation-induced stress is restricted in the damaged subsurface layer.

5. Conclusions

The systematic experimental and modelling works on the FCC single-crystalline pillars of a TWIP steel with the diameter ranging from 3 to 0.5 μm lead to the following conclusions:

1. The flow stress of the present pillars increases considerably with the diameter decreasing from 3 to 0.5 μm, demonstrating a substantial size effect. In particular, a power law was used to fit the yield stress at different diameter, which leads to a power law exponent of 0.43.
2. Detailed microstructure characterization reveals that the plastic deformation of the present pillars is dominated by deformation twinning primarily via twin growth in one single twinning system, indicating that the size effect should be related to deformation twinning instead of dislocation glide.
3. Ion radiation during FIB milling can damage the pillar surface to a depth of several tens of nanometres and induce a high density of vacancy Frank loops into the damaged subsurface layer. Deformation twinning via partial dislocation emission in small-sized FCC crystals may be accomplished by the dissociation of these vacancy Frank loops.
4. Ion radiation can also induce a substantial compressive stress in the damaged subsurface layer, which should facilitate the dissociation of vacancy Frank loops for twinning. Such ion-radiation-induced stress decreases with pillar diameter and therefore leads to the size effect on twinning stress.

Acknowledgements

M.X. Huang is grateful for financial support from the National Science Foundation of China (Grants No. 51301148), the Steel Joint Funds of the National Natural Science Foundation of China (Grant No. U1560204), and the Research Grants Council of Hong Kong (Grants No. 719712, 712713, 17203014).

Appendix A. Supplementary data

Supplementary data related to this article can be found at http://dx.doi.org/10.1016/j.actamat.2017.02.063.

References

[1] E.O. Hall, Twinning and Diffusionless Transformations in Metals, Butterworth, London, 1954.
[2] M.V. Klassen-Neklyudova, Mechanical Twinning of Crystals, Plenum Press, New York, 1964.
[3] P.G. Partridge, The crystallography and deformation modes of hexagonal close-packed metals, Metall. Rev. 12 (1) (1967) 169–194.
[4] S. Mahajan, D.F. Williams, Deformation twinning in metals and alloys, Int. Metall. Rev. 18 (2) (1973) 43–61.
[5] J.W. Christian, S. Mahajan, Deformation twinning, Prog. Mater. Sci. 39 (1995) 1–157.
[6] J.P. Hirth, J. Lothe, Theory of Dislocation, John Wiley & Sons, New York, 1982.
[7] L. Remy, Kinetics of f.c.c. deformation twinning and its relationship to stress-strain behaviour, Acta Metall. 26 (3) (1978) 443–451.
[8] T.W. Kim, Y.G. Kim, Properties of austenitic Fe-25Mn-1Al-0.3C alloy for automotive structural applications, Mater. Sci. Eng. A 160 (2) (1993) 13–15.
[9] O. Bouaziz, S. Allain, C.P. Scott, P. Cugy, D. Barbier, High manganese austenitic twinning induced plasticity steels: a review of the microstructure properties relationships, Curr. Opin. Solid State Mater. Sci. 15 (4) (2011) 141–168.
[10] M.R. Barnett, Twinning and the ductility of magnesium alloys, Mater. Sci. Eng. A 464 (1–2) (2007) 1–7.
[11] M.R. Barnett, Twinning and the ductility of magnesium alloys, Mater. Sci. Eng. A 464 (1–2) (2007) 8–16.
[12] A.A. Salem, S.R. Kalidindi, R.D. Doherty, Strain hardening of titanium: role of deformation twinning, Acta Mater. 51 (14) (2003) 4225–4237.
[13] A.A. Salem, S.R. Kalidindi, S.L. Semiatin, Strain hardening due to deformation twinning in α-titanium: constitutive relations and crystal-plasticity modeling, Acta Mater. 53 (12) (2005) 3495–3502.
[14] Y. Deng, C.C. Tasan, K.G. Pradeep, H. Springer, A. Kostka, D. Raabe, Design of a twinning-induced plasticity high entropy alloy, Acta Mater. 94 (2015) 124–133.
[15] P.F. Yu, H. Cheng, L.J. Zhang, H. Zhang, M.Z. Ma, G. Li, P.K. Liaw, R.P. Liu, Nanotwin's formation and growth in an AlCoCuFeNi high-entropy alloy, Scr. Mater. 114 (2016) 31–34.
[16] Y. Zhang, T.T. Zuo, Z. Tang, M.C. Gao, K.A. Dahmen, P.K. Liaw, Z.P. Lu, Microstructures and properties of high-entropy alloys, Prog. Mater. Sci. 61 (2014) 1–93.
[17] Y.I. Chumlyakov, I.V. Kireeva, O.A. Kutz, A.S. Turabi, H.E. Karaca, I. Karaman, Unusual reversible twinning modes and giant superelastic strains in FeNiCoAlNb single crystals, Scr. Mater. 119 (2016) 43–46.
[18] P. Zhou, Z.Y. Liang, R.D. Liu, M.X. Huang, Evolution of dislocations and twins in a strong and ductile nanotwinned steel, Acta Mater. 111 (2016) 96–107.
[19] O. Bouaziz, Strain-hardening of twinning-induced plasticity steels, Scr. Mater. 66 (12) (2012) 982–985.
[20] H. Fan, S. Aubry, A. Arsenlis, J.A. El-Awady, The role of twinning deformation on the hardening response of polycrystalline magnesium from discrete dislocation dynamics simulations, Acta Mater. 92 (2015) 126–139.
[21] Y.A. Shin, S. Yin, X. Li, S. Lee, S. Moon, J. Jeong, M. Kwon, S.J. Yoo, Y.M. Kim, T. Zhang, H. Gao, S.H. Oh, Nanotwin-governed toughening mechanism in hierarchically structured biological materials, Nat. Commun. 7 (2016) 10772.
[22] S. Alkan, P. Chowdhury, H. Sehitoglu, R.G. Rateick, H.J. Maier, Role of nanotwins on fatigue crack growth resistance – experiments and theory, Int. J. Fatigue 84 (2016) 28–39.
[23] O. Kraft, P.A. Gruber, R. Mönig, D. Weygand, Plasticity in confined dimensions, Annu. Rev. Mater. Res. 40 (1) (2010) 293–317.
[24] W.D. Nix, J.R. Greer, G. Feng, E.T. Lilleodden, Deformation at the nanometer and micrometer length scales: effects of strain gradients and dislocation starvation, Thin Solid Films 515 (6) (2007) 3152–3157.
[25] J.R. Greer, J.T.M. De Hosson, Plasticity in small-sized metallic systems: intrinsic versus extrinsic size effect, Prog. Mater. Sci. 56 (6) (2011) 654–724.
[26] M.D. Uchic, D.M. Dimiduk, J.N. Florando, W.D. Nix, Sample dimensions influence strength and crystal plasticity, Science 305 (2004) 986–989.
[27] M.D. Uchic, P.A. Shade, D.M. Dimiduk, Plasticity of micrometer-scale single crystals in compression, Annu. Rev. Mater. Res. 39 (1) (2009) 361–386.
[28] Q. Yu, Z.-W. Shan, J. Li, X. Huang, L. Xiao, J. Sun, E. Ma, Strong crystal size effect on deformation twinning, Nature 463 (7279) (2010) 335–338.
[29] J. Ye, R.K. Mishra, A.K. Sachdev, A.M. Minor, In situ TEM compression testing of Mg and Mg–0.2wt.% Ce single crystals, Scr. Mater. 64 (3) (2011) 292–295.
[30] J.-H. Seo, H.S. Park, Y. Yoo, T.-Y. Seong, J. Li, J.-P. Ahn, B. Kim, I.-S. Choi, Origin of size dependency in coherent-twin-propagation-mediated tensile deformation of noble metal nanowires, Nano Lett. 13 (11) (2013) 5112–5116.
[31] S.Z. Wu, H.W. Yen, M.X. Huang, A.H.W. Ngan, Deformation twinning in submicron and micron pillars of twinning-induced plasticity steel, Scr. Mater. 67 (7–8) (2012) 641–644.
[32] Y. Lu, J. Song, J.Y. Huang, J. Lou, Surface dislocation nucleation mediated deformation and ultrahigh strength in sub-10-nm gold nanowires, Nano Res. 4 (12) (2011) 1261–1267.
[33] H. Zheng, A. Cao, C.R. Weinberger, J.Y. Huang, K. Du, J. Wang, Y. Ma, Y. Xia, S.X. Mao, Discrete plasticity in sub-10-nm-sized gold crystals, Nat. Commun. 1 (9) (2010) 144.
[34] A. Sedlmayr, E. Bitzek, D.S. Gianola, G. Richter, R. Mönig, O. Kraft, Existence of two twinning-mediated plastic deformation modes in Au nanowhiskers, Acta Mater. 60 (9) (2012) 3985–3993.
[35] G. Dehm, S.H. Oh, P. Gruber, M. Legros, F.D. Fischer, Strain compensation by twinning in Au thin films: experiment and model, Acta Mater. 55 (19) (2007) 6659–6665.
[36] S.H. Oh, M. Legros, D. Kiener, P. Gruber, G. Dehm, In situ TEM straining of single crystal Au films on polyimide: change of deformation mechanisms at the nanoscale, Acta Mater. 55 (16) (2007) 5558–5571.
[37] C. Ji, H.S. Park, Geometric effects on the inelastic deformation of metal nanowires, Appl. Phys. Lett. 89 (18) (2006) 181916.
[38] W. Liang, M. Zhou, Atomistic simulations reveal shape memory of fcc metal nanowires, Phys. Rev. B 73 (11) (2006).
[39] H. Park, K. Gall, J. Zimmerman, Shape memory and pseudoelasticity in metal nanowires, Phys. Rev. Lett. 95 (25) (2005).
[40] H.S. Park, K. Gall, J.A. Zimmerman, Deformation of FCC nanowires by twinning and slip, J. Mech. Phys. Solids 54 (9) (2006) 1862–1881.
[41] E. Rabkin, H.S. Nam, D.J. Srolovitz, Atomistic simulation of the deformation of gold nanopillars, Acta Mater. 55 (6) (2007) 2085–2099.
[42] L.A. Zepeda-Ruiz, B. Sadigh, J. Biener, A.M. Hodge, A.V. Hamza, Mechanical response of freestanding Au nanopillars under compression, Appl. Phys. Lett. 91 (10) (2007) 101907.
[43] J.-H. Seo, Y. Yoo, N.-Y. Park, S.-W. Yoon, H. Lee, S. Han, S.-W. Lee, T.-Y. Seong,

S.-C. Lee, K.-B. Lee, P.-R. Cha, H.S. Park, B. Kim, J.-P. Ahn, Superplastic deformation of defect-free Au nanowires via coherent twin propagation, Nano Lett. 11 (8) (2011) 3499–3502.
[44] Z.Y. Liang, M.X. Huang, Deformation twinning in small-sized face-centred cubic single crystals: experiments and modelling, J. Mech. Phys. Solids 85 (2015) 128–142.
[45] S. Allain, J.P. Chateau, O. Bouaziz, S. Migot, N. Guelton, Correlations between the calculated stacking fault energy and the plasticity mechanisms in Fe–Mn–C alloys, Mater. Sci. Eng. A 387–389 (2004) 158–162.
[46] D.M. Norfleet, D.M. Dimiduk, S.J. Polasik, M.D. Uchic, M.J. Mills, Dislocation structures and their relationship to strength in deformed nickel microcrystals, Acta Mater. 56 (13) (2008) 2988–3001.
[47] D. Kiener, W. Grosinger, G. Dehm, R. Pippan, A further step towards an understanding of size-dependent crystal plasticity: in situ tension experiments of miniaturized single-crystal copper samples, Acta Mater. 56 (3) (2008) 580–592.
[48] W.S. Choi, B.C. De Cooman, S. Sandlöbes, D. Raabe, Size and orientation effects in partial dislocation-mediated deformation of twinning-induced plasticity steel micro-pillars, Acta Mater. 98 (2015) 391–404.
[49] J. Greer, W. Nix, Nanoscale gold pillars strengthened through dislocation starvation, Phys. Rev. B 73 (24) (2006).
[50] R. Dou, B. Derby, A universal scaling law for the strength of metal micropillars and nanowires, Scr. Mater. 61 (5) (2009) 524–527.
[51] P.M. Derlet, R. Maaß, A probabilistic explanation for the size-effect in crystal plasticity, Philos. Mag. 95 (16–18) (2014) 1829–1844.
[52] P.M. Derlet, R. Maaß, Universal power-law strengthening in metals? Scr. Mater. 109 (2015) 19–22.
[53] S.I. Rao, D.M. Dimiduk, M. Tang, M.D. Uchic, T.A. Parthasarathy, C. Woodward, Estimating the strength of single-ended dislocation sources in micron-sized single crystals, Philos. Mag. 87 (30) (2007) 4777–4794.
[54] T.A. Parthasarathy, S.I. Rao, D.M. Dimiduk, M.D. Uchic, D.R. Trinkle, Contribution to size effect of yield strength from the stochastics of dislocation source lengths in finite samples, Scr. Mater. 56 (4) (2007) 313–316.
[55] S.I. Rao, D.M. Dimiduk, T.A. Parthasarathy, M.D. Uchic, M. Tang, C. Woodward, Athermal mechanisms of size-dependent crystal flow gleaned from three-dimensional discrete dislocation simulations, Acta Mater. 56 (13) (2008) 3245–3259.
[56] J.R. Greer, W.C. Oliver, W.D. Nix, Size dependence of mechanical properties of gold at the micron scale in the absence of strain gradients, Acta Mater. 53 (6) (2005) 1821–1830.
[57] Z.W. Shan, R.K. Mishra, S.A. Syed Asif, O.L. Warren, A.M. Minor, Mechanical annealing and source-limited deformation in submicrometre-diameter Ni crystals, Nat. Mater. 7 (2) (2007) 115–119.
[58] T. Zhu, J. Li, Ultra-strength materials, Prog. Mater. Sci. 55 (7) (2010) 710–757.
[59] L.Y. Chen, M. He, J. Shin, G. Richter, D.S. Gianola, Measuring surface dislocation nucleation in defect-scarce nanostructures, Nat. Mater. 14 (2015) 707–714.
[60] A.T. Jennings, J. Li, J.R. Greer, Emergence of strain-rate sensitivity in Cu nanopillars: transition from dislocation multiplication to dislocation nucleation, Acta Mater. 59 (14) (2011) 5627–5637.
[61] A.T. Jennings, J.R. Greer, Heterogeneous dislocation nucleation from surfaces and interfaces as governing plasticity mechanism in nanoscale metals, J. Mater. Res. 26 (22) (2011) 2803–2814.
[62] T. Zhu, J. Li, A. Samanta, A. Leach, K. Gall, Temperature and strain-rate dependence of surface dislocation nucleation, Phys. Rev. Lett. 100 (2) (2008) 025502.
[63] D. Jang, X. Li, H. Gao, J.R. Greer, Deformation mechanisms in nanotwinned metal nanopillars, Nat. Nanotechnol. 7 (9) (2012) 594–601.
[64] G. Richter, K. Hillerich, D.S. Glanola, R. Monlg, O. Kraft, A. Volkert, Ultrahigh strength single crystalline nanowhiskers grown by physical vapor deposition, Nano Lett. 9 (8) (2009) 3048–3052.
[65] H. Bei, S. Shim, E. George, M. Miller, E. Herbert, G. Pharr, Compressive strengths of molybdenum alloy micro-pillars prepared using a new technique, Scr. Mater. 57 (5) (2007) 397–400.
[66] S. Shim, H. Bei, M.K. Miller, G.M. Pharr, E.P. George, Effects of focused ion beam milling on the compressive behavior of directionally solidified micropillars and the nanoindentation response of an electropolished surface, Acta Mater. 57 (2) (2009) 503–510.
[67] D. Kiener, C. Motz, M. Rester, M. Jenko, G. Dehm, FIB damage of Cu and possible consequences for miniaturized mechanical tests, Mater. Sci. Eng. A 459 (1–2) (2007) 262–272.
[68] H. Idrissi, S. Turner, M. Mitsuhara, B. Wang, S. Hata, M. Coulombier, J.P. Raskin, T. Pardoen, G. Van Tendeloo, D. Schryvers, Point defect clusters and dislocations in FIB irradiated nanocrystalline aluminum films: an electron tomography and aberration-corrected high-resolution ADF-STEM study, Microsc. Microanal. Off. J. Microsc. Soc. Am. Microbeam Anal. Soc. Microsc. Soc. Can. 17 (6) (2011) 983–990.
[69] D. Kiener, Z. Zhang, S. Šturm, S. Cazottes, P.J. Imrich, C. Kirchlechner, G. Dehm, Advanced nanomechanics in the TEM: effects of thermal annealing on FIB prepared Cu samples, Philos. Mag. 92 (25–27) (2012) 3269–3289.
[70] J. Marien, J.M. Plitzko, R. Spolenak, R.M. Keller, J. Mayer, Quantitative electron spectroscopic imaging studies of microelectronic metallization layers, J. Microsc. 194 (1999) 71–78.
[71] S. Lee, J. Jeong, Y. Kim, S.M. Han, D. Kiener, S.H. Oh, FIB-induced dislocations in Al submicron pillars: annihilation by thermal annealing and effects on deformation behavior, Acta Mater. 110 (2016) 283–294.
[72] D. Hull, D.J. Bacon, Chapter 5-Dislocations in Face-centered Cubic Metals, Introduction to Dislocations, fifth ed., Butterworth-Heinemann, Oxford, 2011, pp. 85–107.
[73] J. Silcox, P.B. Hirsch, Direct observations of defects in quenched gold, Philos. Mag. 4 (37) (1959) 72–89.
[74] T. Kadoyoshi, H. Kaburaki, F. Shimizu, H. Kimizuka, S. Jitsukawa, J. Li, Molecular dynamics study on the formation of stacking fault tetrahedra and unfaulting of Frank loops in fcc metals, Acta Mater. 55 (9) (2007) 3073–3080.
[75] B.D. Wirth, V. Bulatov, T. Diaz de la Rubia, Atomistic simulation of stacking fault tetrahedra formation in Cu, J. Nucl. Mater. 283–287 (Part 2) (2000) 773–777.
[76] Y.N. Osetsky, A. Serra, M. Victoria, S.I. Golubov, V. Priego, Vacancy loops and stacking-fault tetrahedra in copper, Philos. Mag. A 79 (9) (1999) 2259–2283.
[77] N.M. Rosengaard, H.L. Skriver, Calculated stacking-fault energies of elemental metals, Phys. Rev. B 47 (1992) 865–873.
[78] A. Etienne, M. Hernández-Mayoral, C. Genevois, B. Radiguet, P. Pareige, Dislocation loop evolution under ion irradiation in austenitic stainless steels, J. Nucl. Mater. 400 (1) (2010) 56–63.
[79] S. Punzhin, E. Detsi, A. Kuzmin, J.T.M. De Hosson, Deformation of nanoporous nanopillars by ion beam-induced bending, J. Mater. Sci. 49 (16) (2014) 5598–5605.
[80] L. Romano, N.G. Rudawski, M.R. Holzworth, K.S. Jones, S.G. Choi, S.T. Picraux, Nanoscale manipulation of Ge nanowires by ion irradiation, J. Appl. Phys. 106 (11) (2009) 114316.
[81] A.A. Tseng, Recent developments in nanofabrication using focused ion beams, Small 1 (10) (2005) 924–939.
[82] C. Borschel, S. Spindler, D. Lerose, A. Bochmann, S.H. Christiansen, S. Nietzsche, M. Oertel, C. Ronning, Permanent bending and alignment of ZnO nanowires, Nanotechnology 22 (18) (2011) 185307.
[83] N.S. Rajput, A. Banerjee, H.C. Verma, Electron- and ion-beam-induced maneuvering of nanostructures: phenomenon and applications, Nanotechnology 22 (48) (2011) 485302.
[84] Y.R. Kim, P. Chen, M.J. Aziz, D. Branton, J.J. Vlassak, Focused ion beam induced deflections of freestanding thin films, J. Appl. Phys. 100 (10) (2006) 104322–104330.
[85] N.V. Medhekar, W.L. Chan, V.B. Shenoy, E. Chason, Stress-enhanced pattern formation on surfaces during low energy ion bombardment, J. Phys. Condens. matter Inst. Phys. J. 21 (22) (2009) 224021.